The Impact of Silicon CCD Photon Spread on Quantitative Analyses of Luminescence Images

Daniel Walter, Andreas Fell, Evan Franklin, Daniel Macdonald, Bernhard Mitchell, and Thorsten Trupke

***Abstract*—Commercial and R&D photoluminescence imaging systems commonly employ indirect bandgap silicon charge-coupled device (CCD) imaging sensors. Silicon is a weak absorber of the near-infrared band-to-band emission of silicon, and significant lateral spreading of the luminescence signal can occur within the sensor. Uncorrected, this effect reduces image contrast, introduces artificial signal gradients, and limits the minimum feature size for which accurate quantitative measurements can be derived. Empirical quantification of the spreading effect defined in terms of the point-spread function (PSF) for the imaging apparatus allows for postprocessing deconvolution, which quantitatively improves image accuracy and contrast. Assessment of the impact of a photon spread indicates that signal smear under commonly occurring high contrast ratio scenarios is sufficient to warrant the application of deconvolution to improve the accuracy of quantitative data in calibrated luminescence images. With a carefully defined PSF, corrections to within $\pm$ 10% of the true signal ratio for small-area features can be achieved. Short-pass filtering provides partial correction of the photon spread with the advantage of reduced experimental complexity but, nonetheless, with limitations on the minimum feature size for which accurate signal ratios can be measured.**

***Index Terms*—Calibrated imaging, crystalline silicon, deconvolution, photoluminescence imaging (PLI), point-spread function (PSF).**

I. Introduction

PHOTOLUMINESCENCE imaging (PLI) has rapidly established itself as an invaluable characterization tool for silicon photovoltaic research and development. As a noncontact technique, it can be used to characterize silicon material at all stages of fabrication, from bricks and as-cut wafers to complete solar cells.

The luminescence signal that is generated by a photostimulated silicon wafer has been shown to reveal quantitative, spatially resolved information about effective minority carrier lifetime [1], effective diffusion length [2], dopant density [3], local implied Voc [4], and the concentration of metallic impurities [5], among many other characteristics. That PLI can spatially resolve these details with per-pixel resolutions of as low as several tens of micrometers makes it a powerful tool for revealing subtle points of damage or contamination that would be overlooked by other techniques such as quasi-steady-state photoconductance measurements [6]. Quantitative data extraction from small features in PLI is of enormous value, as small-area features related to a number of different types of defects can be processed with a broad range of parameters on a single sample [7].

Accurately characterizing the luminescence signal at highly localized features is complicated by a number of lateral smearing phenomena in PLI. This study is limited to signal smear in luminescence images as a result of infrared photon spread within the silicon charge-coupled device (CCD) sensor, which only weakly absorbs the near-infrared luminescence spectrum of silicon wafers [8]. It is physically analogous to light trapping within the measured silicon sample but is exacerbated by the relatively thinner active region of the CCD and the small pixel dimensions (approximately 15 μm in the imaging system used in this study). In theoretical treatments of the CCD response to the luminescence spectrum, this characteristic has used a wavelength dependent detection efficiency function modeled after Lambert–Beer absorption. However, such an analysis ignores the impact of luminescence photons that are refracted within the CCD sensor beyond the critical angle. The totally internally reflected infrared photons are capable of travelling many hundreds to thousands of micrometers laterally across the sensor before being absorbed in pixels remote to their initial point of incidence.

The extent of the lateral spread is wavelength dependent. It has thus been previously suggested that short-pass filtering is effective in minimizing this effect [2]. However, even the shorter wavelengths of the emission spectrum are capable of measurable signal spread. For example, the absorption length of a 1000-nm photon in silicon is approximately 160 μm [9], which gives rise to measurable photon spread within the CCD.

Previous studies have described quantitative characterization of the photon spread and the qualitative applications of deconvolution algorithms in postprocessing as a method for contrast enhancement in luminescence images [8], [10]. In this contribution, we extended the analysis to quantitatively observe the impact of photon spread and the achievable restoration via postprocessing in a challenging scenario of a high-contrast, localized feature. In calibrated imaging, such as in effective lifetime imaging, it is the relative level of luminescence signal throughout the

Manuscript received July 17, 2013; revised September 4, 2013; accepted September 27, 2013. Date of publication November 19, 2013; date of current version December 16, 2013.

D. Walter, A. Fell, E. Franklin, and D. Macdonald are with the Centre for Sustainable Energy Systems, Australian National University, Canberra, A.C.T. 2602, Australia (e-mail: daniel.walter@anu.edu.au; andreas.fell@anu.edu.au; evan.franklin@anu.edu.au; Daniel.macdonald@anu.edu.au).

B. Mitchell is with the Australian Centre for Advanced Photovoltaics, School of Photovoltaic and Renewable Energy Engineering, University of New South Wales, Kensington, N.S.W. 2052, Australia (e-mail: bernhard.mitchell@unsw.edu.au).

T. Trupke is with the Australian Centre for Advanced Photovoltaics, School of Photovoltaic and Renewable Energy Engineering, University of New South Wales, Kensington N.S.W. 2052, Australia, and also with BT Imaging Pty. Ltd., Surry Hills, N.S.W. 2010, Australia (e-mail: trupke@gmail.com).

Color versions of one or more of the figures in this paper are available online at http://ieeexplore.ieee.org.

Digital Object Identifier 10.1109/JPHOTOV.2013.2287912

wafer that is the crucial factor. As a result, we focus on the relative variation in signal ratios produced by infrared photon spread.

In this analysis, a number of second-order effects are not considered. These include the spatial dependence of the photon spread and the influence of different correction algorithms under various imaging scenarios. The results presented below are specific to the BT Imaging LIS-R1 PL imaging tool used in this study for imaging silicon wafers of finite thickness. However, similar results have been demonstrated for similar laboratory systems [8], and the methods of analysis are universally applicable.

II. Point-Spread Function

To quantitatively correct for the infrared photon spread, we can apply an elementary technique in image processing known as *deconvolution*. This technique is well established in high-resolution imaging, notably astronomical imaging [11], and exploits a fundamental principle of linear systems, the so-called *superposition principle*. This principle states that the output, or response, of a linear system can be fully described by its response to point-source unit impulses [12].

In optics, this impulse response is more commonly known as the point-spread function (PSF). Translating this to the case of PLI, we can say that the response of our imaging system to an arbitrary luminescence signal can be described by its response to a subpixel point source of luminescence radiation, applied independently to all pixels of the input signal. By measuring the system's characteristic PSF for the silicon luminescence spectrum, we are able to quantify the extent of the signal spread, and subsequently apply postprocessing deconvolution to restore a closer approximation of the true image. In this study, we implement a regularized form of the Richardson–Lucy (RL) algorithm [13], [14] using the ImageJ plugin *Deconvolution Lab* [15]. A more detailed discussion of deconvolution and algorithmic implementations can be found in [11] and [16] or with direct application to PLI in [10].

A. Defining the Point-Spread Function

The technique for measuring the PSF over the necessary dynamic range has been discussed in detail in a previous publication [8]. It is important to determine the PSF experimentally as its definition is strongly dependent on the spectrum of the detected radiation. As the band-to-band luminescence spectrum of silicon is relatively broad, and the exact internal composition of the CCD unknown, the total photon spread is not easily modeled. In this study, images captured with and without a 1020 nm short-pass filter mounted in front of the camera lens are compared. The point source itself is an apertured electroluminescence signal from a high-efficiency silicon solar cell, with the characteristic luminescence spectrum of silicon. Fig. 1 plots the filtered and unfiltered PSFs over the first few orders of magnitude about the center pixel and across the full dynamic range.

Some important conclusions can be drawn from Fig. 1. The first is the need to characterize the PSF over the full physical

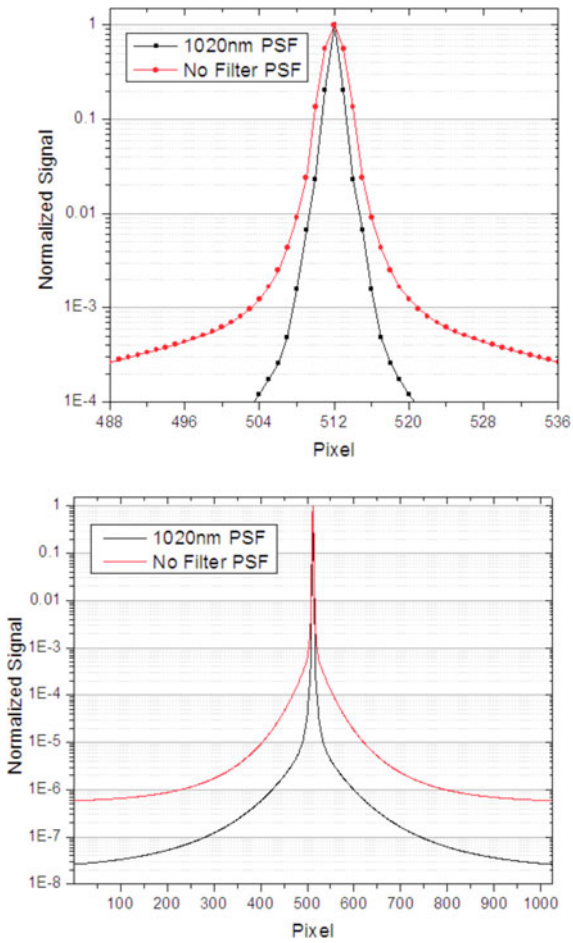

Fig. 1. Comparison of 2-D cross section of PSF with and without short-pass filtering: centered about the point source (top) and the full CCD field of view (bottom).

TABLE I
Proportion of Signal Constrained Within Radii of Point Source

Radius (pixels)	Unfiltered (%)	1020nm SP Filter (%)
1 (centre)	11.9	33.0
10	81.7	93.9
50	91.7	95.7
100	95.1	96.1
500	99.1	99.2

extent of the CCD sensor in order to define the total impact of the photon spread. While the impact of a single pixel on another pixel that is 500 pixels apart may be extremely small ($<10^{-6}$), it is important to note that there is a large number of pixels at that distance, all contributing this small percentage to the remote pixel.

To illustrate the extent of this influence, Table I lists the proportion of total signal measured in a specific pixel over the PL intensity that would be observed in that pixel without smearing within radii between 1 and 500 pixels of the point source. This proportion is defined by the PSFs of Fig. 1. Under both filtering

conditions, considerable spread of signal beyond the center pixel is measured, and we see that for unfiltered imaging, only around 12% of the luminescence signal is captured within the target pixel. As far as 500 pixels from the source pixel, up to 1% of the total signal is still detectable, causing a significant reduction in image contrast if the true signal ratio is sufficiently high, e.g., on the order of 1:100. This overstatement will be further exacerbated by the cumulative signal of numerous source pixels.

Second, it is clear that short-pass filtering results in a measurable reduction in signal smear but, nonetheless, does not provide a complete solution, particularly for pixels in proximity to the luminescence source.

B. Impact of Spectral Variation

The photon spread is a wavelength-dependent effect, and we see from Fig. 1 that with extreme variations in the spectral composition of the detected luminescence spectrum, the characteristic PSFs vary by orders of magnitude. In principle, this means that a PSF would need to be measured for specific sample conditions and may even vary slightly for wafers with different optical properties and minority carrier lifetime. However, in the practical case of wafer imaging, we expect to observe relatively subtle changes in the emission spectrum due to photon reabsorption [17], as differences in wafer quality will affect the steady-state carrier profile. Consequently, simulated PL spectra are presented in Fig. 2, as predicted by 1-D simulations performed by the numerical PV simulation software *Quokka* [18]. Spectra were simulated for a planar 300-μm silicon wafer with bulk lifetimes ranging from 10 to 1000 μs rear illuminated with 808 nm monochromatic illumination with an intensity equivalent to approximately 1 sun illumination (40 mA/cm^2). Luminescence data are calculated using the optical absorption data of Keevers and Green [9]. The respective minority carrier profiles are plotted for reference.

As expected, a reduction in the bulk diffusion length, which results in an asymmetric carrier distribution biased toward the illuminated surface, increases the relative contribution of the short-wavelength portion of the spectrum. However, the maximum variation in relative signal strength between a 10 and a 1000 μs bulk lifetime in the wavelength range of 950 to 1100 nm accounts for a total relative contribution to the emitted spectrum of approximately 2.4%. Fig. 3 plots the ratio of the emission spectra between a bulk lifetime of 10 and 1000 μs as an indication of the extent of this signal variation. However, for bulk lifetimes between 100 and 1000 μs, the total signal variation is less than 2%. The largest discrepancy occurs for bulk lifetimes approaching 1 μs, indicating that for extremely low-lifetime situations (e.g., multicrystalline grain boundaries), spatially varying definitions of the PSF may be required. In higher lifetime wafer imaging scenarios, notably monocrystalline wafers, only a minor variation in the PSF is expected.

C. Impact of Changing Magnification Ratios

The imaging system of this study uses a fixed level of magnification, with a field of view that maps each pixel to an area of approximately 161 by 161 μm at the object plane. In increasing

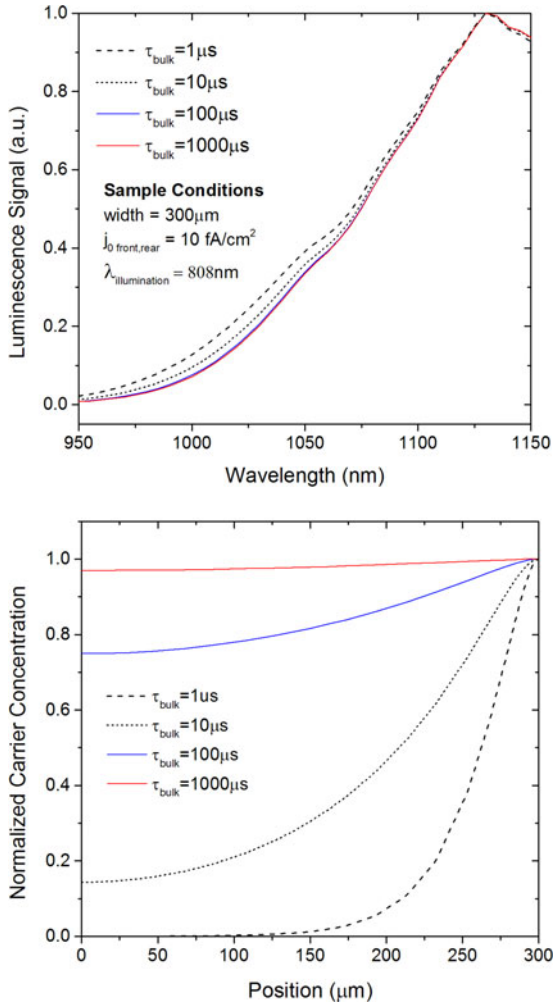

Fig. 2. Normalized silicon luminescence emission spectra for varying bulk lifetime (top) and the corresponding minority carrier profile (bottom) for a range of bulk lifetimes. In the carrier profile plot, the illumination is applied to the right-hand side. The luminescence spectra have been normalized to the peak intensity and the carrier profiles to the carrier concentration at the illuminated surface.

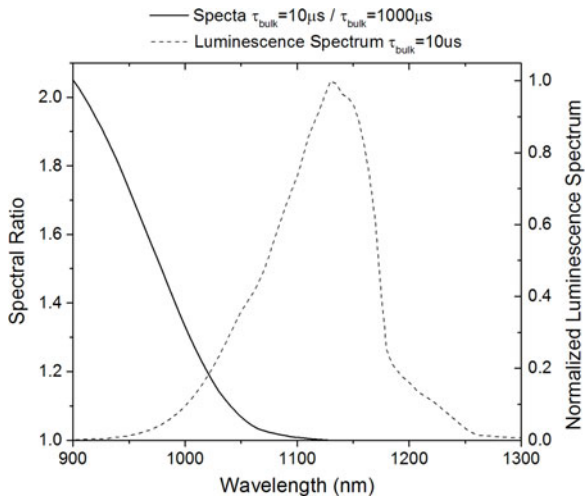

Fig. 3. Ratio of emission spectrum defined as $\tau_{\rm bulk} = 10\ \mu$s/$\tau_{\rm bulk} = 1000\ \mu$s as an indication of relative variation of luminescence flux across spectrum. Overlaid plot of emission spectrum at $\tau_{\rm bulk} = 10\ \mu$s.

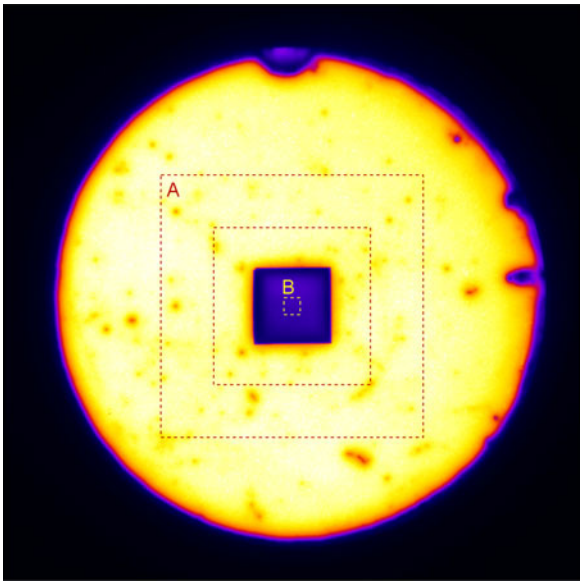

Fig. 4. Luminescence image of test structure for verification of deconvolution algorithm and PSF. The center region has been cut from a second wafer and overlaid on a higher signal substrate wafer. The dashed lines indicate the regions from which the averaged high signal (region A) and low signal (region B) measurements were extracted.

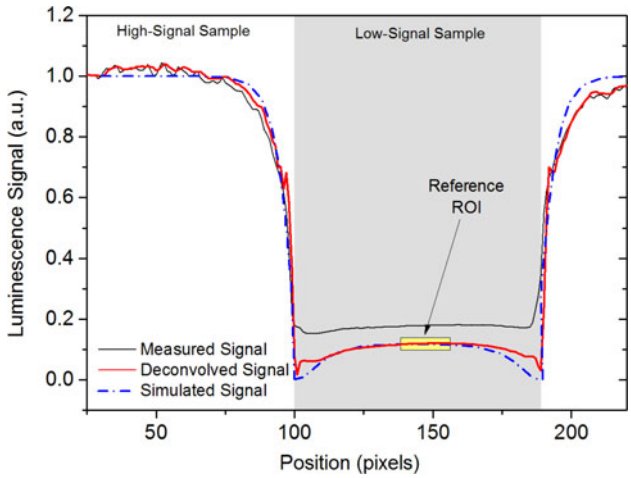

Fig. 5. Cross-sectional profile of measured, deconvolved, and simulated signal profiles under a photon flux (808 nm) of approximately 10^{17} cm^{-2}s^{-1} taken from the luminescence image of Fig. 4. The measured signal profile crosses the two physically separated samples. The signal (carrier) gradient in the region external to the inner low-signal sample can be attributed to the shading and subsequent null generation in this portion of the substrate wafer and is not the result of the CCD-based photon spread. The reference region for the low-signal measurement is indicated.

the level of magnification in the imaging system, it is possible to reduce the extent of the photon smear for an arbitrary feature size by increasing the number of pixels in the CCD that are mapped to that feature. This has a scaling effect on the photon spread, effectively reducing by the level of magnification the feature size for which a similar level of experimental error would be encountered without the magnification. In this study, we have restricted our analysis to a broad field of view, as it is applicable to common full-wafer imaging scenarios.

III. Experimental Validation of Deconvolution

The effect of CCD-based photon spread is a net transfer of signal between pixels, which compresses signal ratios. The accuracy of the restored image depends upon both the PSF and the deconvolution algorithm. However, in order to characterize the quantitative accuracy of the deconvolution method, it is necessary to image a sample of known signal contrast against which the results of the deconvolution can be compared. In this case, a prediction of the detected luminescence signal ratios for two homogenous, symmetrically passivated silicon wafers was simulated with *Quokka*.

The configuration of these two samples is illustrated in Fig. 4, representing an extreme and challenging scenario for accurate signal measurements in the presence of CCD-based photon spread. A small, low-signal region is embedded within a surrounding high-signal region to produce a PL image with a high dynamic range. The imaged samples consist of two semiplanar (Tetramethylammonium hydroxide etched) FZ wafers which were phosphorous gettered [19] to achieve approximately intrinsic bulk lifetimes. To produce differing effective lifetimes, the high-lifetime ($\tau_{\text{eff}} \approx 3$ ms at $\Delta n = 10^{15}$ cm^{-3}) substrate sample is passivated by a high-quality PECVD silicon nitride and the low-lifetime sample ($t_{\text{eff}} \approx 1.1$ ms at $\Delta n = 10^{15}$ cm^{-3}) by a thermal SiO_2 / LPCVD silicon nitride stack. The injection dependent surface recombination is extracted from PCD measurements. Subsequently, a 1.5- cm^2 segment was laser-cut from the lower lifetime sample and overlaid on the high-signal substrate. An intermediate layer of infrared-absorbing film has been added to prevent the center signal being enhanced by the substrate emission. The physical separation of the two samples isolates the CCD-based photon smear effect from wafer-based light trapping and minority carrier diffusion and drift effects.

With a complete characterization of the sample parameters, the ratio of the detected luminescence signals was simulated in *Quokka* by simulating a spatial map of the spectrally resolved luminescence signal, accounting for the measured illumination intensity at 808 nm and an infinite sum of internal reflections. Multidimensional simulations were performed for both samples to account for the shading effects on the substrate wafer and the highly recombination-active edges of the laser-cut center wafer. The injection-dependent lifetime characteristics between the two samples diverged sufficiently to achieve a range of carrier density ratios and consequently area-averaged luminescence signal ratios ranging from approximately 1:7 to 1:24. This was primarily the result of the varying injection dependent surface recombination behavior.

The sample of Fig. 4 was imaged with and without short-pass filtering and subsequently deconvolved using 100 iterations of the RL algorithm. This large number of iterations was chosen to ensure that the final ratio represented the convergent solution of the algorithm. In Fig. 5(a), cross section of the signal profile, overlaid against the simulated ratio under equivalent illumination conditions, is shown. In measuring the signal ratios, the signal of the central feature is extracted within a restricted

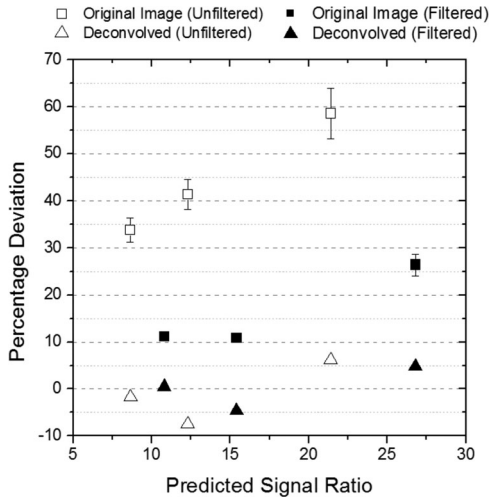

Fig. 6. Percentage deviation of filtered (solid symbols) and unfiltered (open symbols) images before and after deconvolution via 100 iterations of the Richardson–Lucy algorithm for signal ratios ranging between 1:7 and 1:24. Negative deviation indicates that the deconvolved image overstated the predicted ratio. Error bars have been omitted where they do not exceed the size of the symbol.

central region, as indicated in Fig. 4, to limit the influence of edge recombination-induced signal gradient.

In Fig. 6, we plot the percentage deviation of the measured signal ratios from the predicted ratios as calculated by

$$\text{Ratio Deviation (\%)} = \left(1 - \frac{R_{\text{meas}}}{R_{\text{sim}}}\right) \times 100 \qquad (1)$$

where R_{meas} and R_{sim} are the measured and simulated signal ratios, respectively. Following deconvolution, the measured ratios were all restored to within 10% of the predicted ratio; however, in some cases, the restored images produced an overstatement of the true signal ratio. The photon spread contributed to significantly understated signal ratios prior to restoration. The lateral photon spread compressed the signal ratio between the low-signal sample and the surrounding high-signal wafer by approximately 60% in the absence of short-pass filtering and 25% when imaged with the 1020-nm short-pass filter. Of note is how the deconvolution also exposed the signal gradient toward the highly recombination active edges of the inner wafer, the extent of which was not fully revealed in the original, unprocessed image.

IV. Application to Local Feature Characterization

Section III demonstrated an experimental verification of the PSF and the deconvolution technique but measured a relatively large low-signal feature. However, the signal overstatement of the low-signal region will be exacerbated for smaller features and/or large signal ratios. To illustrate the extent of the understatement of the true signal ratios, we convolved the experimental PSFs of Section III with synthetic contrast images equivalent in configuration to the experimental example of Section III (see inset images of Figs. 6 and 7). Under the assumption that these PSFs accurately describe the extent of the photon spread in the CCD sensor, their convolution with the synthetic images provides a theoretical prediction of the impact of the photon spread on the signal ratio.

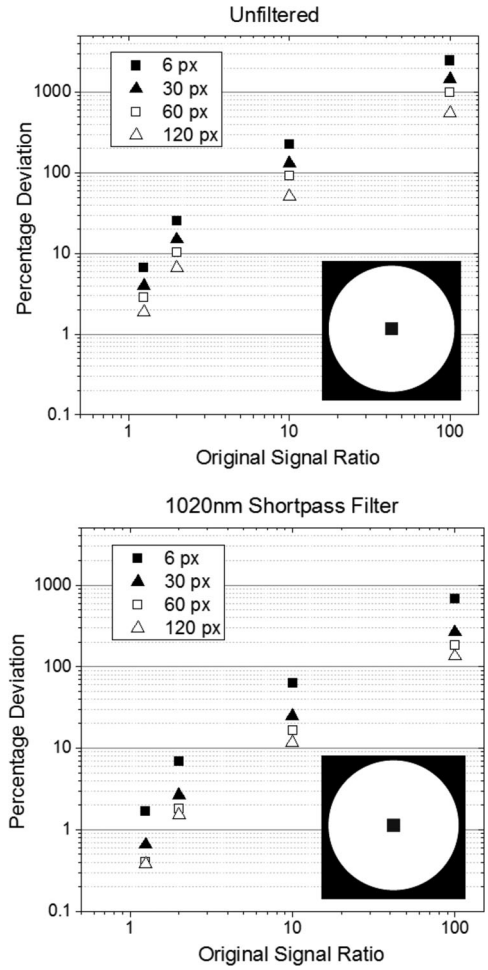

Fig. 7. Percentage overstatement of the signal ratio as a function of the pre-convolution value for a range a feature sizes following convolution of synthetic images with experimental PSFs, both unfiltered (top) and with a 1020-nm short-pass filter (bottom). The inset image illustrates a representative synthetic image prior to convolution.

The central feature was configured with a range of signal ratios with the surrounding "wafer" ranging from 1:1.25 to 1:100 and a range of dimensions between 6 and 120 pixels square (representing approximately 1 to 20 mm for the FOV of the imaging system). Following convolution, the signal from the same regions of interest as illustrated in Fig. 4 were measured and the relative deviation from the true ratio determined as per (1).

Fig. 7 summarizes the extent of the understatement in the total signal ratio. As expected, a reduction in feature size and/or an increase in the total signal ratio increases the deviation in the convolved image from the original signal ratio. While short-pass filtering mitigates the effect to some extent, the signal ratio for any feature size where the true signal ratio exceeds 1:2 is subject to 10% or greater error without deconvolution. In the absence of short-pass filtering, only the combination of the larger features and a contrast level of 1:2 or below restrict the error to within 10%.

V. Conclusion

The weak absorption of silicon luminescence radiation by silicon CCD sensors smears the luminescence signal within the sensor to the extent that as little as 12% of the signal striking each pixel is retained within the pixel. This phenomenon compresses the overall signal ratios within the luminescence image with implications for signal accuracy in quantitative, calibrated luminescence images. The extent of this effect is only partially mitigated by short-pass filtering.

The level of signal inaccuracy under such conditions is a function of the feature size and the true signal contrast but, in the absence of short-pass filtering, can readily exceed 100%. The extent of the signal inaccuracy under such conditions is likely to prove unacceptable for sensitive quantitative imaging applications, particularly when the feature sizes are small relative to surrounding signal regions and a large dynamic range in present.

We observe that characterization of this effect via the imaging system's PSF for the luminescence emission spectrum of silicon allows for post processing deconvolution. By reference to carefully calibrated imaging scenarios, it is demonstrated that deconvolution successfully restores signal ratios to within 10% of their predicted values, even under a challenging scenario of a localized high-contrast signal.

The PSF is sensitive to the spectral composition of the detected signal. However, simulations of the emitted luminescence signal for planar wafers demonstrate that for bulk lifetimes in excess of 10 μs, the spectral composition of the emission spectrum from a finite-thickness silicon wafer under monochromatic illumination is minimally affected, implying a small variation in the PSF. As a result a unique PSF determined for a specific imaging configuration is likely to be suitable for a wide range of sample conditions.

In this analysis, a regularized form of the Richardson–Lucy algorithm was found to produce an accurate first-order correction, but a rigorous comparison of the large number of available deconvolution techniques has not been performed. Further work is recommended to identify a universally optimum combination of PSF and deconvolution algorithm.

References

[1] T. Trupke, R. A. Bardos, M. C. Schubert, and W. Warta, "Photoluminescence imaging of silicon wafers," *Appl. Phys. Lett*., vol. 89, no. 4, pp. 044107-1–044107-3, 2006.

[2] P. Würfel, T. Trupke, and T. Puzzer, "Diffusion lengths of silicon solar cells from luminescence images," *J. Appl. Phys*., vol. 101, no. 12, pp. 123110-1–123110-10, 2007.

[3] S. Lim, M. Forster, X. Zhang, and J. Holtkamp, "Applications of photoluminescence imaging to dopant and carrier concentration measurements of silicon wafers," *IEEE J. Photovoltaics*, vol. 3, no. 2, pp. 649–655, Apr. 2013.

[4] Y. Augarten, B. Tjahjono, T. Trupke, S. Wenham, and B. Hallam, "Photoluminscence imaging for fast determination of the implied open-circuit voltage of silicon wafers," in *Proc. Conf. Rec. 24th Eur. Photovolt. Sol. Energy Conf. Exhib.*, Hamburg, Germany, 2009, pp. 2015–2018.

[5] D. Macdonald, J. Tan, and T. Trupke, "Imaging interstitial iron concentrations in boron-doped crystalline silicon using photoluminescence," *J. Appl. Phys*., vol. 103, no. 7, pp. 073710-1–073710-7, 2008.

[6] M. D. Abbott, J. E. Cotter, F. W. Chen, T. Trupke, R. A. Bardos, and K. C. Fisher, "Application of photoluminescence characterization to the development and manufacturing of high-efficiency silicon solar cells," *J. Appl. Phys*., vol. 100, no. 11, pp. 114514-1–114514-10, 2006.

[7] A. Fell, D. Walter, S. Kluska, and K. Weber, "Determination of injection dependent recombination properties of locally processed surface regions," *Energy Procedia*, vol. 38, pp. 22–31, 2013.

[8] B. Mitchell, J. W. Weber, D. Walter, D. Macdonald, and T. Trupke, "On the method of photoluminescence spectral intensity ratio imaging of silicon bricks: Advances and limitations," *J. Appl. Phys*., vol. 112, no. 6, pp. 063116-1–063116-13, 2012.

[9] M. A. Green and M. J. Keevers, "Optical properties of intrinsic silicon at 300 K," *Prog. Photovoltaics Res. Appl*., vol. 3, no. 3, pp. 189–192, 1995.

[10] D. Walter, A. Liu, E. Franklin, D. Macdonald, B. Mitchell, and T. Trupke, "Contrast enhancement of luminescence images via point-spread deconvolution," in *Proc. 38th IEEE Photovolt. Spec. Conf*., Austin, TX, USA, 2012, pp. 307–312.

[11] J. L. Starck and E. Pantin, "Deconvolution in astronomy: A review," *Publ. Astron. Soc. Pac*., vol. 114, no. 800, pp. 1051–1069, 2002.

[12] J. W. Goodman, *Introduction to Fourier Optics*. Greenwood Village, CO, USA: Roberts, 2005, ch. 2, pp. 3–29.

[13] W. Richardson, "Bayesian-based iterative method of image restoration," *J. Opt. Soc. Amer. A*., vol. 62, no. 1, pp. 55–59, 1972.

[14] L. Lucy, "An iterative technique for the rectification of observed distributions," *Astron. J*., vol. 79, no. 4, pp. 745–754, 1974.

[15] C. Vonesch and M. Unser, "A fast thresholded landweber algorithm for wavelet-regularized multidimensional deconvolution," *IEEE Trans. Image Process*., vol. 17, no. 4, pp. 539–549, Apr. 2008.

[16] R. Gonzalez, *Digital Image Processing*. Boston, MA, USA: Prentice–Hall, 2007.

[17] T. Trupke, "Influence of photon reabsorption on quasi-steady-state photoluminescence measurements on crystalline silicon," *J. Appl. Phys*., vol. 100, no. 6, pp. 063531-1–0635318, 2006.

[18] A. Fell, "A free and fast three-dimensional/two-dimensional solar cell simulator featuring conductive boundary and quasi-neutrality approximations," *IEEE Trans. Electron Devices*, vol. 60, no. 2, pp. 733–738, Feb. 2013.

[19] S. Phang and D. Macdonald, "Direct comparison of boron, phosphorus, and aluminum gettering of iron in crystalline silicon," *J. Appl. Phys*., vol. 109, no. 7, pp. 073521-1–073521-6, 2011.

Authors' photographs and biographies not available at the time of publication.